

Surface wave height distributions and rogue wave probabilities on two-layer fluids

Johannes Gemmrich * and Tom Redhead 

Department of Physics and Astronomy, University of Victoria, Victoria, BC, Canada V8W 2Y2

Adam Monahan 

School of Earth and Ocean Sciences, University of Victoria, Victoria, BC, Canada V8P 3E6



(Received 13 January 2023; accepted 21 April 2023; published 19 May 2023)

The distribution of wave heights, and therefore the occurrence rate of extreme waves, depends on the shape of the surface elevation spectrum. In an idealized two-layer flow, e.g., fresh water overlaying salt water, the spectral shape of surface waves is modified by class-three triad interactions. We conduct numerical simulations of the wave field evolution on a two-layer stratified fluid. Starting from realistic deep-water JONSWAP spectra, the spectral density at high wavenumbers increases while the variance in the peak region decreases and the peak shifts slightly lower. The enhancement of the spectral tail grows rapidly with increasing initial wave steepness and is strongest for broad-banded spectra. Monte Carlo simulations of surface realizations are performed, where the surface is a linear superposition of wave components taken from the initial and the modified spectra. In all cases, the wave height and crest height distributions can be expressed by modified Rayleigh distributions. On a two-layer flow the probability of rogue waves can be up to two orders of magnitude lower than in the unstratified deep-water case, whereas the probability of rogue crests is nearly unaffected. The average crest-trough correlation, calculated from the spectra, is a good predictor for rogue wave probabilities even for strongly modified spectra with enhanced high-wavenumber spectral variance.

DOI: [10.1103/PhysRevFluids.8.054804](https://doi.org/10.1103/PhysRevFluids.8.054804)

I. INTRODUCTION

Large ocean waves may cause serious damage to ships, offshore platforms, and coastal structures, and understanding the occurrence rate of large waves is important for maritime safety [1]. The risk associated with large waves depends on the absolute height of a wave as well as how extreme the wave is relative to the prevailing sea state. Due to the stochastic nature of individual wave heights, exceedance probabilities are the best way to assess the risk presented by an ocean sea state.

The prevailing sea state is characterized by the significant wave height H_s , defined as the average of the largest third of the waves in the wave field. An individual wave is defined as the profile of the surface elevation between two consecutive downward zero crossings at a fixed location. The wave height H is the distance from the peak (or crest) of the profile to the trough, and the crest height η is the distance from the mean water level to the wave crest [2]. Wave height exceedance probability is the probability that a given wave will exceed some value, often expressed as multiples

*Gemmrich@uvic.ca

of the significant wave height H_s :

$$P(z) = \text{prob}\left(\frac{H}{H_s} \geq z\right). \quad (1)$$

In deep water gravity waves are dispersive and at any given location the wave field is a superposition of individual wave components of varying frequency and direction. Based on linear theory the resulting wave height distributions are given by the Rayleigh distribution [3], and for narrow-banded spectra their exceedance probability is

$$P\left(\frac{H}{H_s} > z\right) = e^{-2z^2} \quad \text{and} \quad P\left(\frac{\eta}{H_s} > z\right) = e^{-8z^2} \quad (2)$$

for wave heights and crest heights, respectively.

More generally, the exceedance probability can be written as a Weibull distribution:

$$P\left(\frac{H}{H_s} > z\right) = \exp\left(\frac{-z^\alpha}{\beta_H}\right), \quad P\left(\frac{\eta}{H_s} > z\right) = \exp\left(\frac{-z^\alpha}{\beta_\eta}\right). \quad (3)$$

where α and β are functions of the spectral bandwidth, and water depth [4]. For a discussion of common parametrizations for (3), see [5]. Besides these theoretically derived wave statistics a wide range of empirical distributions have been developed, as reviewed in [6].

The transformation

$$\ln[-\ln(P)] = \alpha \ln(z) - \ln(\beta) \quad (4)$$

results in straight lines of the exceedance probability (3) when plotted against $\ln(z)$ and deviations from the linear model are easily recognized [5]. Observed wave height distributions show good agreement with the Weibull distribution up to moderate normalized wave heights H/H_s , but a sharp increased probability for extreme waves [7–9]. Monte Carlo simulations of random superposition of fourth-order Stokes waves showed excellent agreement with real ocean wave height distributions, including the increased probability of extreme waves [5,8,9]. Thus, for idealized conditions of a narrow-banded wave field on homogeneous deep water the wave height distribution is reasonably well known. However, on stratified water the wave spectra, and therefore the wave height distribution might be different.

The commonly weak density stratification in the ocean supports internal waves which can generate converging and diverging weak currents at the surface. The resulting wave-current interactions affect mainly the high wavenumber tail of the surface wave spectrum, making internal waves highly visible in remote sensing synthetic aperture radar images (e.g., [10]). Modulations of the surface wave spectra can be significant, up to $O(1)$, but are restricted to wave length of order 1 m, or less [11], and will therefore have a negligible impact on the wave height distribution.

On the other hand, oceanic conditions with a shallow well-mixed surface layer having a lower density than the underlying water can be idealized as a two-layer flow. Such a two-layer flow supports so-called class-three wave-wave triad interactions between two surface waves and an interfacial wave, all propagating in the same direction [12]. These triad wave-wave interactions are limited to wavenumbers $k > k_c$, where the critical wavenumber k_c increases with decreasing density difference between the two layers. For large density differences the critical wavenumber is comparable to the wavenumber k_p at the peak of the wave spectrum and the triad interaction results in a downshift of the peak [13]. In oceanic conditions the density difference between the two layers can be due to temperature and salinity, with salinity generally taking a more dominant role. For example, a layer of fresh water overlaying oceanic salt water occurs naturally in estuaries or due to freshly melted sea ice. In such a situation a realistic lower bound for the density ratio $R = \rho_u/\rho_l$ is $R = 0.97$, where ρ_u, ρ_l are the densities of the upper and lower layer, respectively, and $k_c = 8.3k_p$.

Recent simulations of waves on an idealized two-layer stratified water body using high-order spectral methods (HOS) [14] show the evolution of the wave spectrum in the case of

$R = 0.97$ [15]. The simulations predict an overall energy decrease with a relative enhancement of the high-wavenumber tail of the spectrum. Here we analyze what is the effect of this profound change of the spectral shape on the resulting wave height distribution.

II. SIMULATION OF WAVE FIELD EVOLUTION

We consider a two-layer system with a shallow upper layer and a deep lower layer with thickness h_u, h_l , respectively, and $h_u \ll h_l$. Such a system can support gravity waves at the free surface and at the interface between the two layers, both propagating in the positive x direction. The model is described in detail in [12,13,15]. Here we give a basic summary.

The irrotational motion is obtained from Laplace's equation for the velocity potentials $\Phi_u(x, z, t)$ in the upper layer and $\Phi_l(x, z, t)$ in the lower layer, where z denotes the vertical coordinate direction:

$$\nabla^2 \Phi_u = 0, \quad -h_u + \eta_l < z < \eta_u, \quad (5a)$$

$$\nabla^2 \Phi_l = 0, \quad -h_u - h_l < z < -h_u + \eta_l. \quad (5b)$$

The kinematic boundary conditions are

$$\frac{\partial \eta_u}{\partial t} + \frac{\partial \eta_u}{\partial x} \frac{\partial \Phi_u}{\partial x} - \frac{\partial \Phi_u}{\partial z} = 0, \quad z = \eta_u, \quad (6a)$$

$$\frac{\partial \eta_l}{\partial t} + \frac{\partial \eta_l}{\partial x} \frac{\partial \Phi_u}{\partial x} - \frac{\partial \Phi_u}{\partial z} = 0, \quad z = -h_u + \eta_l, \quad (6b)$$

$$\frac{\partial \eta_l}{\partial t} + \frac{\partial \eta_l}{\partial x} \frac{\partial \Phi_l}{\partial x} - \frac{\partial \Phi_l}{\partial z} = 0, \quad z = -h_u + \eta_l. \quad (6c)$$

The dynamic boundary conditions are given by the Bernoulli equation:

$$\frac{\partial \Phi_u}{\partial t} + \frac{1}{2} \left[\left(\frac{\partial \Phi_u}{\partial x} \right)^2 + \left(\frac{\partial \Phi_u}{\partial z} \right)^2 \right] + g\eta_u = 0, \quad z = \eta_u, \quad (7a)$$

$$\rho_u \left\{ \frac{\partial \Phi_u}{\partial t} + \frac{1}{2} \left[\left(\frac{\partial \Phi_u}{\partial x} \right)^2 + \left(\frac{\partial \Phi_u}{\partial z} \right)^2 \right] + g\eta_l \right\} - \rho_l \left\{ \frac{\partial \Phi_l}{\partial t} + \frac{1}{2} \left[\left(\frac{\partial \Phi_l}{\partial x} \right)^2 + \left(\frac{\partial \Phi_l}{\partial z} \right)^2 \right] + g\eta_l \right\} = 0, \quad z = -h_u + \eta_l, \quad (7b)$$

$$\frac{\partial \Phi_l}{\partial z} = 0, \quad z = -h_u - h_l, \quad (7c)$$

where g is the acceleration due to gravity, and η_u and η_l are the elevations of the surface and the interface, respectively, composed of the superposition of small amplitude plane waves.

The system (5)–(7) can be expanded into a set of evolution equations:

$$\frac{\partial \eta_u}{\partial t} = -\frac{\partial \eta_u}{\partial x} \frac{\partial \Phi_u^S}{\partial x} + \left[1 + \left(\frac{\partial \eta_u}{\partial x} \right)^2 \right] \frac{\partial \Phi_u}{\partial z}, \quad z = \eta_u, \quad (8a)$$

$$\frac{\partial \Phi_u^S}{\partial t} = -\frac{1}{2} \left[\left(\frac{\partial \Phi_u^S}{\partial x} \right)^2 - \left[1 + \left(\frac{\partial \eta_u}{\partial x} \right)^2 \right] \left(\frac{\partial \Phi_u}{\partial z} \right)^2 \right] - g\eta_u, \quad z = \eta_u, \quad (8b)$$

$$\frac{\partial \eta_l}{\partial t} = -\frac{\partial \eta_l}{\partial x} \frac{\partial \Phi_u^I}{\partial x} + \left[1 + \left(\frac{\partial \eta_l}{\partial x} \right)^2 \right] \frac{\partial \Phi_u}{\partial z}, \quad z = -h_u + \eta_l, \quad (8c)$$

$$\frac{\partial \Psi^I}{\partial t} = \frac{1}{2} \left[R \left(\frac{\partial \Phi_u^I}{\partial x} \right)^2 - \left(\frac{\partial \Phi_l^I}{\partial z} \right)^2 \right] + \frac{1}{2} \left[1 + \left(\frac{\partial \eta_l}{\partial x} \right)^2 \right] \left[\left(\frac{\partial \Phi_l}{\partial z} \right)^2 - R \left(\frac{\partial \Phi_u}{\partial z} \right)^2 \right] - g\eta_l(1 - R), \quad z = -h_u + \eta_l, \quad (8d)$$

where $\Phi_u^S(x, t) = \Phi_u(x, \eta_u, t)$ and $\Psi^I(x, t) = \Phi_u(x, -h_u + \eta_l, t) - R \Phi_l(x, -h_u + \eta_l, t)$. This system can be solved with the HOS method [16]. Similar to Gemmrich and Monahan [15], we restrict the expansion to second order in wave steepness.

The single boundary conditions at the *a priori* unknown time- and space-varying surface, $z = \eta_u(x, t)$, and interface, $z = -h_u + \eta_l(x, t)$, are transformed into a series of linearized boundary conditions for the perturbed potentials $\Phi_u^{(m)}$ and $\Phi_l^{(m)}$, $m = 1, 2$ at fixed vertical locations, which can be solved sequentially, starting from $m = 1$. Using a fourth-order Runge-Kutta scheme for integration, the time-varying surface and interfacial elevations and their velocity potentials at all locations x are obtained. After each time step the “wave-breaking scheme” described in Gemmrich and Monahan [15] reduces steep waves to the Stokes limiting steepness 0.14.

The model is nondimensionalized with mean upper layer depth, lower layer density, and acceleration due to gravity as scaling parameters. We initialize the model with a realistic surface wave field and let it evolve over a period of 1000 dominant wave periods T_p . This duration is long enough for class-three triad interactions to generate interfacial waves [12] and to achieve nearly steady-state solutions.

Two-layer conditions in the ocean are most likely in fetch-limited conditions and a Joint North Sea Wave Project (JONSWAP) type spectrum [17] is a suitable choice for initial surface wave spectra. The frequency-domain JONSWAP spectrum is implemented in the MATLAB toolbox WAFO [18]:

$$S_s(\omega) = \frac{b H_s^2}{\omega_p} \left(\frac{\omega_p}{\omega} \right)^5 \exp \left[-\frac{5}{4} \left(\frac{\omega}{\omega_p} \right)^{-4} \right] \gamma^q, \quad (9)$$

$$q = \exp \left(-\frac{1}{2} \frac{(\omega/\omega_p - 1)^2}{s} \right)$$

with normalization factor b , peak frequency ω_p , and $s = 0.07$ for $\omega \leq \omega_p$ and $s = 0.09$ for $\omega > \omega_p$. The peak enhancement factor γ is a measure of wave field development, ranging from $\gamma = 1$ for fully developed seas to $\gamma = 7$ for young seas. We then convert the dimensional frequency-domain spectrum $S(\omega)$ into its nondimensional wavenumber form $S(k/k_p)$ based on the deep-water dispersion relation $\omega^2 = k g$. The model (8) is evaluated at $N_x = 2^{21}$ evenly spaced locations where the initial surface elevation is a random realization consistent with the initial wavenumber spectrum. The interface between the two layers is initially undisturbed. The evolution of the surface and the interface are then calculated for a duration of 1000 dominant wave periods T_p , at a time step $\Delta t = T_p/500$.

To cover a wide range of sea states we run the two-layer model (8) for 56 initial conditions, specified by $R = 0.97$, $\omega_p = 2\pi$, $\gamma = [1, 2, 3, 4, 5, 6, 7]$, and nondimensional wave heights $H_s = [0.02, 0.03, 0.04, 0.05, 0.06, 0.07, 0.08, 0.09]$. Each run is repeated six times with different seeds for the random number generation, i.e., the initial surface wave fields have identical spectral shapes but six different realizations. These 56 initial conditions result in different average wave steepness ak , which is mainly governed by the value of H_s , and different spectral bandwidth

$$v = \left(\frac{m_0 m_2}{m_1^2} - 1 \right)^{1/2}, \quad (10)$$

where m_n is the n th moment of the spectrum [19].

Here we are interested in the changes of the spectral shape of the surface wave field, due to class-three triad interactions and associated wave breaking. Except for very small wave heights, and therefore small average wave steepness ak , the surface wave spectrum undergoes the following three changes: (i) a weak downshift of the peak, (ii) an overall loss of power, and (iii) a pronounced enhancement of the spectral tail, $k > 3k_p$. Modifications of the spectral shape in the peak region $0.5k_p < k < 3k_p$ are strongest for more developed sea states, i.e., smaller γ (Fig. 1).

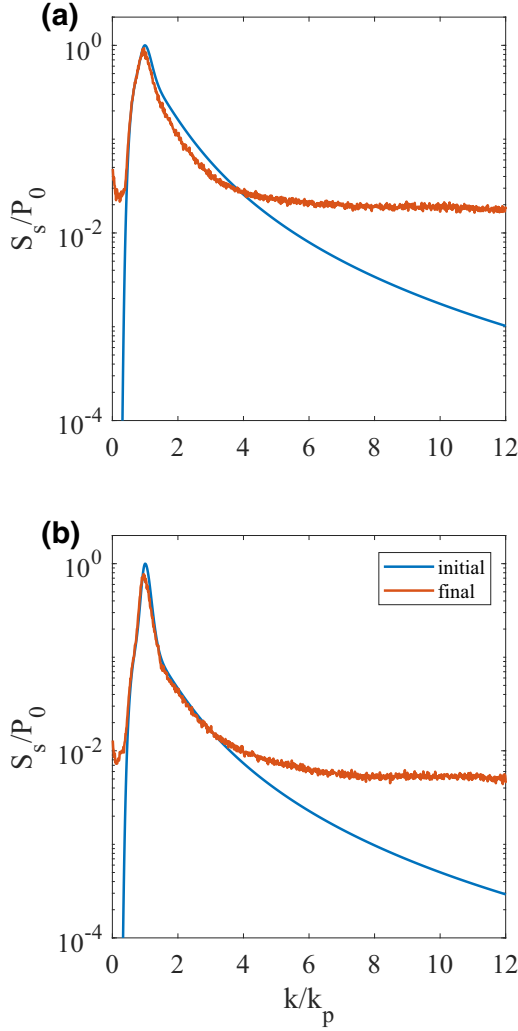


FIG. 1. Evolution of normalized surface wave spectra from initial condition (blue) to condition at $t = 1000T_p$ (red); $H_s = 0.07$. (a) $\gamma = 2$. (b) $\gamma = 7$.

The surface energy dissipated during the evolution of the two-layer flow is a combination of energy transfer to the interface displacement and dissipation due to wave breaking [15]. It can be quantified as

$$\Gamma_s = \frac{\rho_u \left[\int_0^{k_{\max}} S_s(k, t = 0) dk - \int_0^{k_{\max}} S_s(k, t = 1000) dk \right]}{\rho_u \int_0^{12k_p} S_s(k, t = 0) dk}. \quad (11)$$

Here we chose $k_{\max} = 12k_p$. This choice ensures that the initial spectral density at $k > k_{\max}$ is negligible, $S(k_{\max}, t = 0)/S(k_p, t = 0) < 10^{-3}$, while $k_{\max} \gg k_{\text{crit}}$.

Energy dissipation Γ_s shows a strong threshold behavior on wave steepness with little dissipation at $ak < 0.07$ and 20%–30% dissipation for the steepest initial conditions $0.12 < ak < 0.14$. Its dependence on spectral bandwidth does not appear to be systematic [Fig. 2(a)].

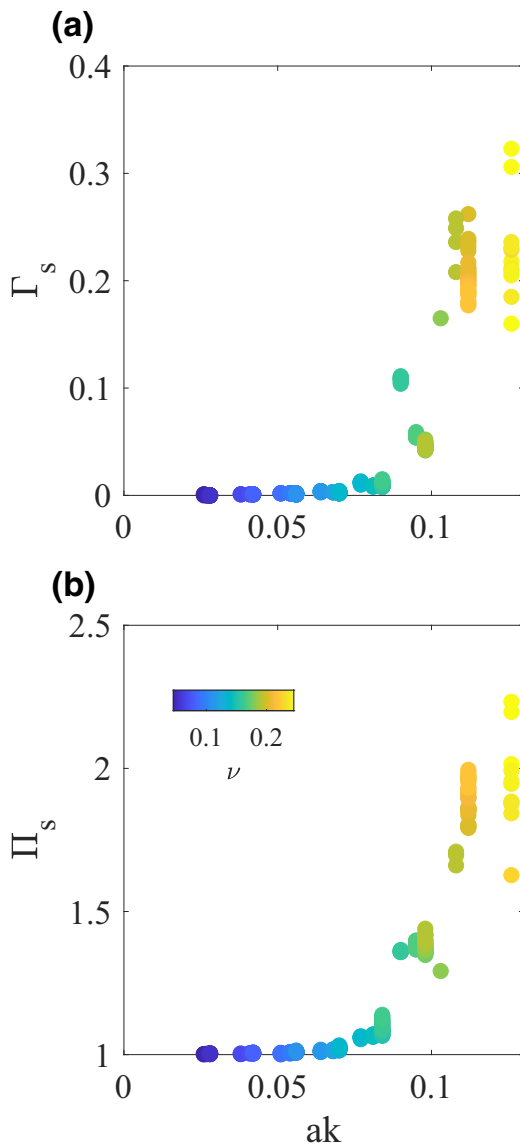


FIG. 2. Relative change of spectral surface wave energy after $1000T_p$ as a function of initial dominant wave steepness ak and initial spectral bandwidth ν . (a) Energy loss Γ_s . (b) Spectral tail enhancement Π_s .

The strongest impact of the triad interactions is the enhancement of the spectral tail. This can be quantified as tail enhancement:

$$\Pi_s = \frac{E_{\text{tail}}(t = 1000)}{E_{\text{peak}}(t = 1000)} \left(\frac{E_{\text{tail}}(t = 0)}{E_{\text{peak}}(t = 0)} \right)^{-1}, \quad (12)$$

where

$$E_{\text{peak}}(t) = \int_0^{2.5k_p} S_s(k, t) dk, \quad E_{\text{tail}}(t) = \int_{2.5k_p}^{k_{\text{max}}} S_s(k, t) dk. \quad (13)$$

The tail enhancement shows a strong threshold behavior on wave steepness, similar to the energy dissipation [Fig. 2(b)]. In addition, Π_s is positively correlated with spectral bandwidth ν . For steep waves, $ak > 0.11$, the total variance in the spectral tail, $k > 2.5k_p$, approximately doubles, $\Pi_s \approx 2$, compared to the initial JONSWAP conditions.

III. SURFACE WAVE HEIGHT DISTRIBUTIONS

To evaluate the impact these profound spectral changes, Γ_s , Π_s , have on the distribution of wave heights we perform Monte Carlo simulations of surface elevations:

$$\eta_u(x) = \sum_{n=1}^{N_k} a_n \cos(k_n x) + b_n \sin(k_n x). \quad (14)$$

The coefficients a_n , b_n are generated from a normal distribution, have zero mean, and a variance equal to the desired spectrum at k_n . Surface elevations are generated from the initial spectrum, and the evolved spectrum at $t = 1000T_p$, for each set of (γ, H_s) parameters of the two-layer simulations. The spectra are evaluated at $N_k = 2^{22}$ wavenumbers. This yields about 2×10^5 individual waves for each realization, from which the normalized wave heights H/H_s and crest heights η/H_s are extracted, where the significant wave height $H_s = 4\sigma_{\eta_u}$ is calculated separately for each realization. This procedure is repeated 100 times with different random seeds, but the same spectrum. Since for each initial condition the two-layer evolution (8) is run six times, there are six sets of slightly different spectra. The Monte Carlo simulations of surface elevations are then repeated for the additional runs of the two-layer evolution (8) for the given initial condition, resulting in 600 synthetic surface elevation records for each initial (γ, H_s) . In total there are roughly 10^8 individual wave and crest heights from which the exceedance probability can be calculated. Examples of initial and final wave height and crest height distributions are given in Figs. 3(a) and 4(a).

It is well known that higher-order Stokes corrections, responsible for sharper and taller crests, and shallower and flatter troughs, result in several orders of magnitude increase in the probability of extreme wave heights, resulting in curved lines for $H/H_s \gtrsim 2.2$ when plotted according to (4) [5]. To highlight the effect of two-layer wave field evolution we purposely restrict our analysis to purely linear simulations, without Stokes corrections. For linear simulations the exceedance probability curves are expected to be straight lines and deviations are easily determined.

The exceedance probability P of wave heights for any given value $H/H_s \leq 2.5$ decreases for waves on a two-layer flow compared to the initial JONSWAP condition [Fig. 3(a)]. The initial as well as the final wave height distribution follow a Weibull distribution (3), as expected for linear superposition and indicated by a straight line (4), with $\alpha(\text{initial}) = \alpha(\text{final}) \approx 2$, and $\beta_H(\text{final}) < \beta_H(\text{initial}) \approx 1/2$. The decrease in β implies that the relative change in wave height exceedance probability increases with normalized wave height z . The change in the wave height distribution is linked to the energy dissipation and the tail enhancement during the two-layer evolution. Therefore, it is not surprising that the relative change of exceedance probability, quantified by the ratio $P(z)_{\text{final}}/P(z)_{\text{initial}}$, shows a threshold behavior on average wave steepness, similar to Γ_s and Π_s [Fig. 3(b)]. For example, the likelihood of rogue waves, defined as $z \geq 2.2$, decreases by roughly 10% in moderate steep initial conditions, $ak < 0.1$, but in the steepest conditions, $ak > 0.12$, their occurrence rate is expected to drop by almost two orders of magnitude.

In contrast, the distribution of normalized crest heights η/H_s is nearly identical for the initial and the evolved spectra (Fig. 4). Only the most extreme crests $\eta/H_s > 1.15$ show a small increase of exceedance probabilities at the evolved stage. For the steepest initial wave fields the likelihood of rogue crests, commonly defined as $\eta/H_s > 1.25$, increase by up to a factor 1.4 [Fig. 4(b)], much smaller than the order of magnitude change of rogue wave probabilities [Fig. 3(b)].

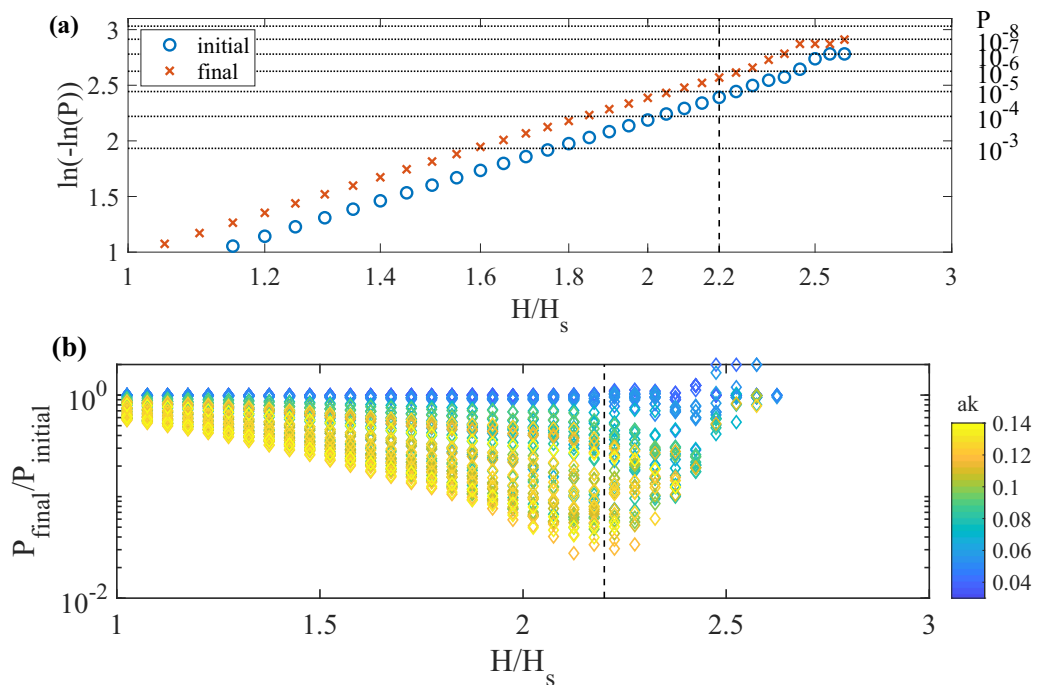


FIG. 3. (a) Wave height distribution probability P for initial spectrum (blue \circ) and final spectrum at $t = 1000$ (red \times); $\gamma = 5$; $H_s = 0.08$. (b) Relative change in wave height exceedance probabilities for all cases, stratified by the dominant initial wave steepness ak . Dashed vertical line indicates the rogue wave criterion.

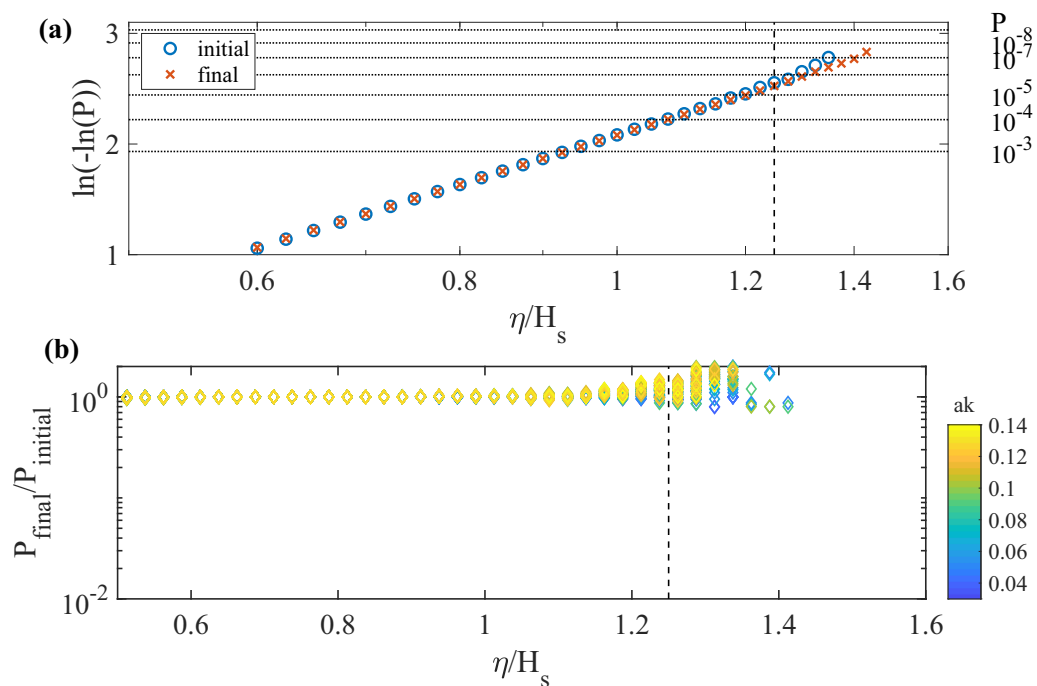


FIG. 4. Same as Fig. 3, but for crest height.

IV. CREST-TROUGH CORRELATION

The different evolution for wave height and crest height distributions implies a decrease in the average correlation r between crests and the following troughs. If the crest heights were strongly correlated with the trough depths a large crest height would also have a large trough depth in most cases. Since a wave height is just the sum of the crest height and the trough depth, a large crest height and large trough depth would equal a large wave height. As such, the only way for crest heights to show such different behavior from the corresponding wave heights is if the crest heights became decoupled from the trough depths. This difference in crest heights versus trough depths is not related to nonlinearities or higher-order Stokes corrections [20] since the surface elevation (14) is a linear superposition of independent, Gaussian-distributed components.

The probability of a large wave occurring, assuming a sufficiently narrow bandwidth, is larger for strongly correlated crest heights and trough depths [21,22]. Additionally, the Rayleigh exceedance curve (2) is calculated assuming that each wave height is twice the corresponding crest height [21]. This assumption is equivalent to perfectly correlated crest heights and trough depths, $r = 1$. For finite but narrow bandwidth the exceedance probability for wave heights is given by a modified Rayleigh distribution [23]:

$$P\left(\frac{H}{H_s} > z\right) = \exp\left(\frac{-2z^2}{\beta_r}\right), \quad \beta_r = \frac{1+r}{2}, \quad (15)$$

where the crest-trough correlation r is defined with trough depths taken to be positive, i.e., $r = 1$ implying perfectly correlated crests and troughs.

A recent analysis of more than 1×10^9 individual waves [24] confirmed the crest-trough correlation as the strongest predictor for wave height exceedances for $z = 2.0$ and $z = 2.4$ [22], and r could build the basis for a practical probabilistic rogue wave prediction. However, the calculation of the crest-trough correlation requires the height and depth of the individual crest-trough pairs, which are often not available. A proxy can be the average correlation at the dominant wave period [25]:

$$\tilde{r} = \frac{1}{m_0} \sqrt{\rho^2 + \lambda^2},$$

with

$$\begin{aligned} \rho &= \int_0^\infty S(f) \cos(2\pi f\tau) df, \\ \lambda &= \int_0^\infty S(f) \sin(2\pi f\tau) df, \end{aligned} \quad (16)$$

where $\tau = \frac{\bar{T}}{2}$ is the lag time at half the spectral mean period $\bar{T} = \frac{m_0}{m_1}$, and m_n is the n th spectral moment.

The advantage of using \tilde{r} is that it can be readily calculated not only from the full surface elevation record η but also from more widely available observed one-dimensional wave spectra, and from standard wave model output [9].

Here we calculate $\tilde{r}_{\text{initial}}$, \tilde{r}_{final} according to (16) from the initial and final frequency spectra, respectively. For all our simulations the initial crest-trough correlation is relatively high, $0.67 < \tilde{r}_{\text{initial}} < 0.82$, and the correlations corresponding to the final spectra are generally less than the initial, $\tilde{r}_{\text{final}} \leq \tilde{r}_{\text{initial}}$. As a result of the wave field evolution on the two-layer fluid the probability of rogue waves, $P(H/H_s > 2.2)$, decreases on average as the decline of the final crest-trough correlation becomes more prominent [Fig. 5(a)]. However, for a given decline in correlation \tilde{r} the reduction of rogue wave probability can vary by up to one order of magnitude, especially for $\tilde{r}_{\text{initial}} - \tilde{r}_{\text{final}} > 0.2$, with no consistent dependence on the actual value of the correlation, or the wave steepness (not shown). In a real-world two-layer flow the initial crest-trough correlation would not be known, only \tilde{r}_{final} . However, the modified Rayleigh distribution (15) provides a reasonable

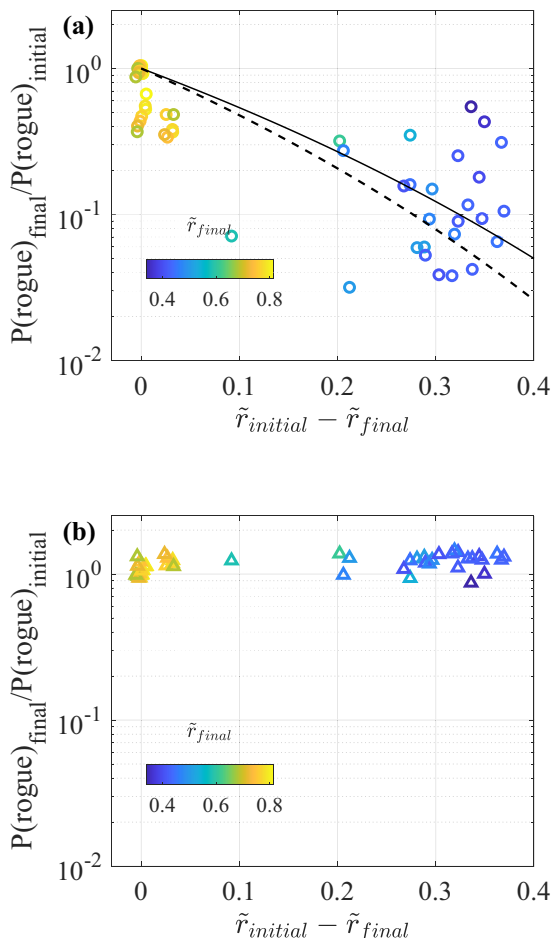


FIG. 5. Change of probability of (a) rogue waves $[P(H/H_s > 2.2)]$ and (b) rogue crests $[P(\eta/H_s > 1.25)]$, as a function of change in crest-trough correlation \tilde{r} , stratified by final crest-trough correlation \tilde{r}_{final} . Lines represent (15) for $\tilde{r}_{\text{initial}} = 0.82$ (solid) and $\tilde{r}_{\text{initial}} = 0.67$ (dashed).

approximation of our scattered simulation data with only weak dependence on the value $\tilde{r}_{\text{initial}}$ of the crest-trough correlation in the unstratified case [Fig. 5(a)].

As discussed above, the probability of large crests can increase slightly in a two-layer situation for very steep initial wave fields [Fig. 4(b)]. However, the change in probabilities of rogue crests $P(\eta/H_s > 1.25)$ does not depend on the crest-trough correlation, as expected [Fig. 5(b)].

Rogue waves (rogue crests) are rare events that populate the tail of the wave height (crest height) distribution, and therefore their probabilities are particularly sensitive to sampling variability. Our simulations are based on six realizations for each parameter setting. We expect that by substantially increasing the number of realizations the large scatter of rogue wave probabilities would be reduced, and the apparent weak dependence of rogue crest probabilities on \tilde{r}_{final} would disappear.

V. CONCLUSIONS

Situations of a shallow layer of nearly fresh water overlaying a deep layer of salt water resulting in a density ratio $R = 0.97$ are the limiting case of idealized two-layer flows in the ocean. Even such small density changes can support class-three wave triad interactions between two surface waves

and an interfacial wave. These three-wave interactions, which are not possible in deep unstratified water, result in a spectral tail enhancement of the surface wave field. This modification of the shape of the surface spectrum has a significant effect on the distribution of individual wave heights, and only a weak effect on the distribution of crest heights.

Our analysis is restricted to purely linear waves, neglecting higher-order Stokes corrections. Thus, absolute occurrence rates of rogue waves would not be representative for real ocean conditions. However, the ratio of rogue wave probabilities in the two-layer system to the unstratified case provides an estimate of the relative effect of stratification on rogue wave occurrence. Our simulations show a decrease of rogue wave probabilities in the two-layer flow by up to two orders of magnitude, and a much smaller increase of rogue crests, up to a factor 1.4.

In deep, unstratified water the crest-trough correlation r evaluated at half the mean wave period is a good predictor for rogue wave probabilities. The modified Rayleigh distribution, which includes r as a correction, accounts for finite bandwidth effects [23]. The same correction is valid in the two-layer case, even for strongly modified spectra with enhanced high wavenumber spectral variance.

These results are based on idealized simulations and need testing in real-world conditions. A first step should be the analysis of the spectral tail of the wave field in estuaries, or in polar conditions following ice melt. Since the spectral modifications are expected to be most visible at high wave numbers, say $k > 5k_p$, high sampling rates and an extremely low noise floor are required for such measurements. Another pronounced feature of waves on a two-layer fluid will be the reduced probability of extreme individual waves but a nearly unaffected probability of extreme crests. Therefore, a strong mismatch between rogue wave occurrence and rogue crest occurrence in wave observations in potential two-layer conditions would be a strong indication for the spectral modifications predicted by the model. Such observations have to be of sufficient length, say several weeks, to show a significantly higher number of extreme crests than extreme waves. While it is unlikely for a two-layer stratification due to melt water to remain for such a long period, observations in estuaries would be a strong candidate to look for the asymmetry of rogue wave and rogue crest occurrences.

ACKNOWLEDGMENTS

Funding for this project was provided by the Marine Environmental Observation, Prediction and Response (MEOPAR) network's modeling core. The computations were performed on West-Grid/Compute Canada [26].

-
- [1] I. Nikolkina and I. Didenkulova, Rogue waves in 2006–2010, *Nat. Hazards Earth Syst. Sci.* **11**, 2913 (2011).
 - [2] L. H. Holthuijsen, in *Waves in Oceanic and Coastal Waters* (Cambridge University Press, Cambridge, UK, 2007), p. 387.
 - [3] M. S. Longuet-Higgins, On the statistical distribution of the heights of sea waves, *J. Mar. Res.* **11**, 245 (1952).
 - [4] G. Z. Forristall, Wave crest distributions: Observations and second-order theory, *J. Phys. Oceanogr.* **30**, 1931 (2000).
 - [5] J. Gemmrich and C. Garrett, Dynamical and statistical explanations of observed occurrence rates of rogue waves, *Nat. Hazards Earth Syst. Sci.* **11**, 1437 (2011).
 - [6] E. Vanem, T. Zhu, and A. Babanin, Statistical modelling of the ocean environment—A review of recent developments in theory and applications, *Marine Struct.* **86**, 103297 (2022).
 - [7] K. Dysthe, H. E. Krogstad, and P. Müller, Oceanic rogue waves, *Annu. Rev. Fluid Mech.* **40**, 287 (2008).
 - [8] J. Gemmrich and J. Thomson, Observations of the shape and group dynamics of rogue waves, *Geophys. Res. Lett.* **44**, 1823 (2017).

- [9] J. Gemmrich and L. Cicon, Generation mechanism and prediction of an observed extreme rogue wave, *Sci. Rep.* **12**, 1718 (2022).
- [10] R. Romeiser and H. C. Graber, Advanced remote sensing of internal waves by spaceborne along-track InSAR—A demonstration with TerraSAR-x, *IEEE Trans. Geosci Remote Sens.* **53**, 6735 (2015).
- [11] L. Lenain and N. Pizzo, Modulation of surface gravity waves by internal waves, *J. Phys. Oceanogr.* **51**, 2735 (2021).
- [12] M.-R. Alam, A new triad resonance between co-propagating surface and interfacial waves, *J. Fluid Mech.* **691**, 267 (2012).
- [13] M. Tanaka and K. Wakayama, A numerical study on the energy transfer from surface waves to interfacial waves in a two-layer fluid system, *J. Fluid Mech.* **763**, 202 (2015).
- [14] D. G. Dommermuth and D. K. P. Yue, A high-order spectral method for the study of nonlinear gravity waves, *J. Fluid Mech.* **184**, 267 (1987).
- [15] J. Gemmrich and A. Monahan, Surface and interfacial waves in a strongly stratified upper ocean, *J. Phys. Oceanogr.* **51**, 269 (2021).
- [16] M.-R. Alam, Y. Liu, and D. K. P. Yue, Bragg resonance of waves in a two-layer fluid propagating over bottom ripples. Part II. Numerical simulation, *J. Fluid Mech.* **624**, 225 (2009).
- [17] K. Hasselmann, T. Barnett, E. Bouws, H. Carlson, D. Cartwright, K. Enke, J. Ewing, H. Gienapp, D. Hasselmann, P. Kruseman, A. Meerburg, P. Müller, D. Olbers, K. Richter, W. Sell, and H. Walden, Measurements of wind-wave growth and swell decay during the Joint North Sea Wave Project (JONSWAP), *Deutsche Hydrographische Zeitschrift, Ergänzungsheft Reihe A* **8**, 1 (1973).
- [18] P. Brodtkorb, P. Johannesson, G. Lindgren, I. Rychlik, J. Rydén, and E. Sjö, WAFO - A Matlab toolbox for the analysis of random waves and loads, in *Proceedings of the Tenth International Offshore and Polar Engineering Conference (ISOPE)*, Seattle, Washington, USA (International Society of Offshore and Polar Engineers, 2000), Vol. 3, pp. 343–350.
- [19] M. S. Longuet-Higgins, Statistical properties of wave groups in a random sea state, *Philos. Trans. R. Soc. London, Ser. A* **312**, 219 (1984).
- [20] G. G. Stokes, Supplement to a paper on the theory of oscillatory waves, in *Mathematical and Physical Papers* (Cambridge University Press, Cambridge, UK, 1880), pp. 314–326.
- [21] M. Casas-Prat and L. H. Holthuijsen, Short-term statistics of waves observed in deep water, *J. Geophys. Res.* **115**, C9 (2010).
- [22] D. Häfner, J. Gemmrich, and M. Jochum, Real-world rogue wave probabilities, *Sci. Rep.* **11**, 10084 (2021).
- [23] A. Naess, On the distribution of crest to trough wave heights, *Ocean Eng.* **12**, 221 (1985).
- [24] D. Häfner, J. Gemmrich, and M. Jochum, FOWD: A free ocean wave dataset for data mining and machine learning, *J. Atmos. Ocean. Technol.* **38**, 1305 (2021).
- [25] M. A. Tayfun and F. Fedele, Wave-height distributions and nonlinear effects, *Ocean Eng.* **34**, 1631 (2007).
- [26] www.computecanada.ca.